MIT Libraries | DSpace@MIT

MIT Open Access Articles

Growth Dynamics During Dropwise Condensation on Nanostructured Superhydrophobic Surfaces

The MIT Faculty has made this article openly available. ***Please share*** how this access benefits you. Your story matters.

Citation: Miljkovic, Nenad, Ryan Enright, and Evelyn N. Wang. "Growth Dynamics During Dropwise Condensation on Nanostructured Superhydrophobic Surfaces." ASME 2012 Third International Conference on Micro/Nanoscale Heat and Mass Transfer 3-6 March 3, 2012, Atlanta, Georgia, USA, ASME, 2012. © 2012 by ASME.

As Published: http://dx.doi.org/10.1115/MNHMT2012-75278

Publisher: ASME International

Persistent URL: http://hdl.handle.net/1721.1/120301

Version: Final published version: final published article, as it appeared in a journal, conference proceedings, or other formally published context

Terms of Use: Article is made available in accordance with the publisher's policy and may be subject to US copyright law. Please refer to the publisher's site for terms of use.

Massachusetts Institute of Technology

Proceedings of the ASME 2012 3rd Micro/Nanoscale Heat & Mass Transfer International Conference
MNHMT2012
March 3-6, 2012, Atlanta, Georgia, USA

MNHMT2012-75278

GROWTH DYNAMICS DURING DROPWISE CONDENSATION ON NANOSTRUCTURED SUPERHYDROPHOBIC SURFACES

Nenad Miljkovic[1], Ryan Enright[1,2], Evelyn N. Wang[1]
[1]Device Research Laboratory, Massachusetts Institute of Technology, Cambridge, MA, USA
[2]Stokes Institute, University of Limerick, Limerick, Ireland

ABSTRACT

Condensation on superhydrophobic nanostructured surfaces offers new opportunities for enhanced energy conversion, efficient water harvesting, and high performance thermal management. Such surfaces are designed to be Cassie stable, which minimize contact line pinning and allow for passive shedding of condensed water droplets at sizes smaller than the capillary length. In this work, we investigated *in situ* water condensation on superhydrophobic nanostructured surfaces using environmental scanning electron microscopy (ESEM). The "Cassie stable" surfaces consisted of silane coated silicon nanopillars with diameters of 300 nm, heights of 6.1 μm, and spacings of 2 μm, but allowed droplets of distinct suspended (S) and partially wetting (PW) morphologies to coexist. With these experiments combined with thermal modeling of droplet behavior, the importance of initial growth rates and droplet morphology on heat transfer is elucidated. The effect of wetting morphology on heat transfer enhancement is highlighted with observed 6× higher initial growth rate of PW droplets compared to S droplets. Consequently, the heat transfer of the PW droplet is 4-6× higher than that of the S droplet. To compare the heat transfer enhancement, PW and S droplet heat transfer rates are compared to that of a flat superhydrophobic silane coated surface, showing a 56% enhancement for the PW morphology, and 71% degradation for the S morphology. This study provides insight into importance of local wetting morphology on droplet growth rate during superhydrophobic condensation, as well as the importance of designing CB stable surfaces with PW droplet morphologies to achieve enhanced heat transfer during dropwise condensation.

INTRODUCTION

Condensation on superhydrophobic nanostructured surfaces has received significant attention in the past few decades to enhance heat and mass transfer by passively shedding water droplets at length scales smaller than the capillary length [1]. Previous studies have focused on designing and fabricating superhydrophobic surfaces that can achieve spontaneous droplet removal during condensation [2-8]. These surfaces are energetically favorable to form Cassie droplets [2, 8, 9] which reside on the air filled nanostructures and have little contact line pinning to the surface as compared to Wenzel droplets which wet the cavities of the nanostructure [10]. However, recent studies have identified that different wetting morphologies can exist on Cassie stable surfaces where partial wetting of the base occurs beneath the Cassie droplet [11, 12]. To elucidate the importance of such differences, studies on droplet growth dynamics are needed, which have in general been ignored.

In this work, we investigated *in situ* water condensation on superhydrophobic nanostructured surfaces using environmental scanning electron microscopy (ESEM). The superhydrophobic nanostructured surfaces were designed to be "Cassie stable", but allowed droplets of distinct suspended (S) and partially wetting (PW) morphologies to coexist on the surface. With these experiments combined with thermal modeling of droplet behavior, the importance of initial growth rates and droplet morphology on heat transfer is elucidated. Consequently, the heat transfer of the PW and S droplet morphologies were characterized and compared with that of a flat superhydrophobic surface providing insight into the importance of local wetting morphology on droplet growth rate during superhydrophobic condensation.

EXPERIMENTAL DESIGN AND CHARACTERIZATION

Nanostructured Surface Preparation

Silicon nanopillar surfaces [Fig. 1(a)] with diameters of d = 300 nm, heights of h = 6.1 μm, center-to-center spacings of l = 2 μm where the solid fraction is $\varphi = \pi d^2/4l^2 = 0.018$ and

Copyright © 2012 by ASME

Downloaded From: https://proceedings.asmedigitalcollection.asme.org on 01/09/2019 Terms of Use: http://www.asme.org/about-asme/terms-of-use

roughness factor is $r = 1 + \pi dh/l^2 = 3.26$ were fabricated using e-beam lithography and deep reactive ion etching (DRIE). The samples were first cleaned in a plasma cleaner (*Harrick Plasma*) for 20 minutes, then placed in a vacuum chamber containing an open container of silane and held at roughing vacuum levels for 30 minutes. Upon removal from the chamber the samples were rinsed in ethanol, DI water, and then dried with N_2. Goniometer measurements on a smooth silanated silicon surface showed advancing and receding contact angles of θ_a = 119.2° ± 1.3° and θ_r = 86.1° ± 1.3°, respectively, resulting in a calculated equilibrium angle of θ_e = 102.1° ± 1.4°.

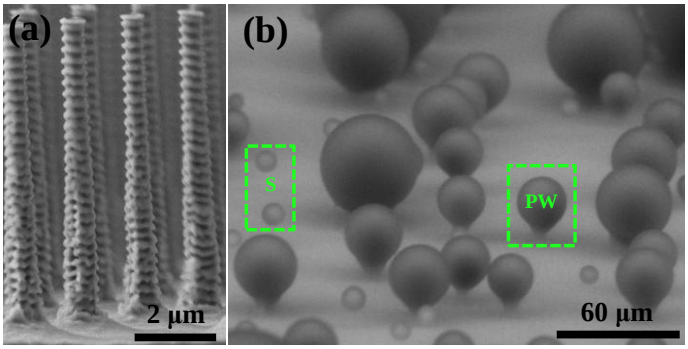

Fig. 1. *(a) Scanning electron micrographs (SEM) of an array of superhydrophobic silicon nanopillars with diameters, heights, and spacings of d = 300 nm, h = 6.1 μm, and l = 2 μm, respectively. (b) Environmental scanning electron micrographs (ESEM) of water condensation on (a) showing both partially wetting (PW) and suspended (S) droplets (P = 1200 ± 12 Pa, T_s = 282 ± 1.5 K).*

An energy-based criterion can be defined to delineate the expected condensing droplet morphology on the fabricated nanostructured surface [13], given by

$$E^* = \frac{\cos\theta^{CB}}{\cos\theta^{W}} = \frac{-1}{r\cos\theta_a}. \quad (1)$$

When $E^* > 1$ the contact line near the base of the pillars can overcome the energy barrier to de-pin and a Wenzel droplet is formed. If $E^* < 1$ complete de-pinning is not possible and the droplet spreads over the top of the pillar array forming a nominally Cassie Baxter droplet as $R \gg l$. This interpretation is consistent with the behavior observed in Fig. 1b where after accounting for the scallop features on the pillar sides as $h' = (\pi/2)h$ [14], we calculate $E^* = 0.63$.

ESEM Experiments

Droplet growth on the surfaces was characterized using an environmental scanning electron microscope (*Zeiss EVO 55 ESEM*). Back scatter detection mode was used with a high gain. The water vapor pressure in the ESEM chamber was 1200 ± 12 Pa. The sample temperature was set to 9 ± 1.5 °C using a cold stage resulting in nucleation of water droplets on the sample surface due to condensation of the saturated water vapor. Typical image capture was obtained with a beam potential of 20 kV and variable probe current depending on stage inclination angle. To limit condensed droplet heating effects [11] probe currents were kept below 2.9 nA and view area was kept above 400 x 300 μm^2. Images and recordings were obtained at an inclination angle of 70 to 80 degrees from the horizontal to observe growth and wetting dynamics close to the droplet base. Copper tape was used for mounting the sample to the cold stage to ensure good thermal contact.

Fig. 1(b) shows the two distinct droplet morphologies, PW and S droplets on the surface. PW droplets nucleate within a unit cell and while growing beyond the confines beyond the unit cell, they spread across the tops of the pillars in the shape of a balloon with a pinned neck in the pillars. Before coalescence with neighboring droplets, an increasing proportion of the droplet contact area is in the composite state and has an increasing apparent contact angle which approaches $\theta_{PW} = 164 \pm 4°$ for $\langle R \rangle$ > 15 μm [Fig 2(a)]. It is important to note, the PW droplet morphology is distinct from the classical Wenzel morphology by only locally wetting the substrate beneath the droplet center. S droplets nucleate and grow on top of the pillars in a spherical shape with an apparent contact angle of $\theta_S = 164 \pm 6°$ [Fig 2(b)]. The measured contact angles are in good agreement with the calculated $\theta_{CB} = 170.6°$ using the Cassie-Baxter equation, $\cos\theta_{CB} = \varphi(\cos\theta_e + 1) - 1$, where θ_e is the intrinsic equilibrium contact angle. At these droplet sizes (~ 1 - 10 μm), such a wetting configuration is typically energetically unfavorable due to a Laplace pressure instability mechanism [15], but may be attributed to the presence of scallop features on the pillar sides that pin the contact line.

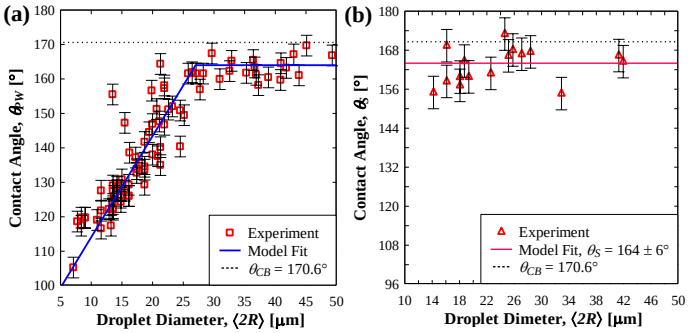

Fig. 2. *Droplet contact angle as a function of diameter for the (a) PW morphology. The model fit is defined as $\theta_{PW}(R) = 85° + 5.82R°$ for ⟨2R⟩ ≤ 27 μm, and $\theta_{PW} = 164°$ for ⟨2R⟩ > 27 μm. (b) S morphology.*

During the condensation process, droplet removal *via* coalescence induced jumping [1, 16] was observed. The average coalescence droplet diameter (l_c) at steady state was determined to be 10 ± 2 μm, which is 30× smaller than the droplet capillary length. The spontaneous out of plane droplet motion is a result of the surface energy released upon in plane droplet coalescence [Fig. 3]. Both PW and S droplets were observed to have equal probability for coalescence, indicating the contact line pinning force for both droplet morphologies is comparable.

Copyright © 2012 by ASME

Downloaded From: https://proceedings.asmedigitalcollection.asme.org on 01/09/2019 Terms of Use: http://www.asme.org/about-asme/terms-of-use

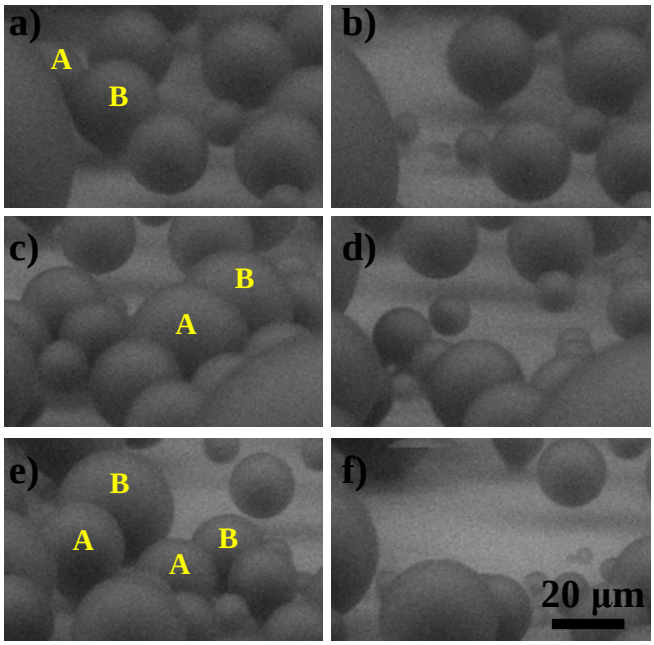

Fig. 3. *Coalescence induced droplet ejection for three separate locations. Images a), c) and e) show the condensing droplet surfaces prior to coalescence, while images b), d) and f) show the corresponding surfaces after coalescence and ejection. Labels A and B are used to denote the coalescing droplets. For clarity, the three cases shown are all large droplet diameter coalescence events exceeding the average coalescence diameter of 10 ± 2 µm [6].*

Figure 4 shows time lapse images of both PW and S droplets, which highlight the drastic differences in droplet morphology and growth rates on the surface. The experimentally obtained average droplet diameters as a function of time for the PW and S morphologies prior to coalescence and spontaneous removal are shown in Figures 6(a) and (b), respectively. The growth rate of the S droplet is initially 6× lower than that of the PW droplet for $\langle R \rangle$ < 6 µm. As the droplets reach radii $\langle R \rangle$ > 6 µm, the growth rates for both morphologies are comparable which suggests that the mechanism limiting droplet growth for both wetting states at the later stages are the same.

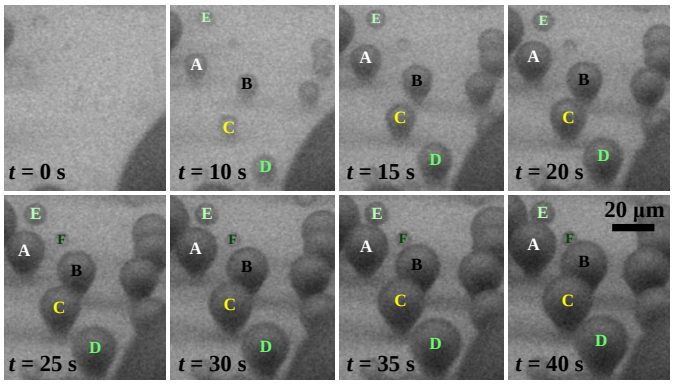

Fig 4. *Time lapse images of condensation captured via ESEM video showing the difference in growth behavior between PW and S droplets. Droplets A, B, C, and D are in the PW state, whereas E and F are in the S state.*

MODEL DEVELOPMENT

To provide insight into the experimental results and capture the growth dynamics of the different morphologies, we developed a thermal resistance based heat transfer model [17] which accounts for the presence of hydrophobic pillar structures. Figure 5(a) shows schematics of the PW and S droplets with the associated parameters used in a thermal resistance model. The heat is first transferred from saturated vapor to the liquid-vapor interface through resistances associated with droplet curvature (R_c) and liquid-vapor interface (R_i). The heat is conducted through the droplet and pillar structure to the substrate through resistances due to droplet conduction (R_d), hydrophobic coating (R_{hc}), pillars (R_p) and the gap (R_g). Marangoni and buoyant induced convection within the droplet were neglected in the model because the droplets were assumed to be sufficiently small so that conduction is the primary mode of heat transfer [18, 19]. Each thermal resistance is related to a temperature drop in the resistance network. The temperature drop is due to droplet curvature [20] (ΔT_C) given by

$$\Delta T_C = \frac{R^*}{R}(T_{sat} - T_s) = \frac{2T_{sat}\sigma}{Rh_{fg}\rho_w}, \quad (2)$$

where T_{sat} is the water vapor saturation temperature, σ is the water surface tension, h_{fg} is the latent heat of vaporization, and ρ_w is the water condensate density.

The temperature drop between the saturated vapor and liquid interface (ΔT_i) is given by

$$\Delta T_i = T_{sat} - T_i = \frac{q}{h_i 2\pi R^2(1-\cos\theta)}, \quad (3)$$

where q is the heat transfer rate through the droplet and h_i is the condensation interfacial heat transfer coefficient [21, 22] given by

$$h_i = \frac{2\alpha}{2-\alpha}\frac{1}{\sqrt{2\pi\bar{R}T_s}}\frac{{h_{fg}}^2}{v_g T_s}, \quad (4)$$

where $\bar{R}$ is the gas constant, v_g is the water vapor specific volume. The condensation coefficient, α, is the ratio of vapor molecules that will be captured by the liquid phase to the total number of vapor molecules striking the liquid surface, ranging from 0 to 1. We assumed α = 0.9 which is appropriate for clean environments such as the ESEM [20]. However, for this study, the model results were not sensitive to the condensation coefficient ranging from 0.1 to 1.

Once heat is transferred to the droplet interface, it must conduct through the droplet from the interface to the base. This leads to a droplet conduction temperature drop (ΔT_d) given by [17]

$$\Delta T_d = T_i - T_{b1} = \frac{q\theta}{4\pi R k_w \sin\theta}, \quad (5)$$

where T_{b1} is the liquid temperature of the droplet base and k_w is the water thermal conductivity.

Copyright © 2012 by ASME

Downloaded From: https://proceedings.asmedigitalcollection.asme.org on 01/09/2019 Terms of Use: http://www.asme.org/about-asme/terms-of-use

The temperature drop due to the hydrophobic coating is calculated via a conduction resistance given by

$$\Delta T_{HC} = T_{b1} - T_{b2} = \frac{q\delta_{HC}}{\varphi\pi R^2 k_{HC}\sin^2\theta}, \quad (6)$$

where T_{b2} is the temperature of the silicon pillars beneath the hydrophobic coating, δ_{HC} is the hydrophobic coating thickness (δ_{HC} = 1 nm), φ is the structured surface solid fraction, and k_{HC} is the coating thermal conductivity (k_{HC} = 0.2 W/mK).

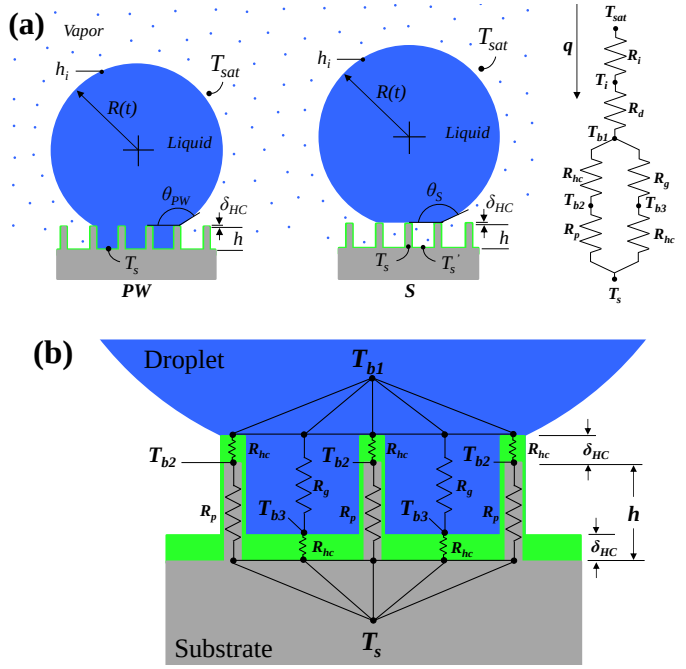

Fig. 5. *(a) Schematics of a PW and S droplet and the associated thermal resistance diagram showing the liquid-vapor interface (R_i), droplet conduction (R_d), hydrophobic coating (R_{hc}), pillar (R_p) and gap (R_g) thermal resistances. (b) Thermal resistance network of the pillar structure. The schematic outlines the parallel path of heat flowing through i) the hydrophobic coating (R_{hc}) followed by the pillar (R_p) and ii) the liquid bridge (R_g) followed by the coating (R_{hc}).*

The conduction resistance through the pillars is dependent on the wetting mode of the droplet. If the droplet morphology is suspended (S), the conduction resistance is given by

$$\Delta T_{P,S} = T_{b2} - T_s = \frac{qh}{\varphi\pi R^2 k_P \sin^2\theta}, \quad (7)$$

where T_s is the structured surface substrate temperature, h is the structured surface pillar height (h = 6.1 μm), and k_P is the pillar thermal conductivity (k_P = 150 W/mK).

If the droplet morphology is PW, the conduction resistance temperature drop through the pillar and coating structure is calculated by considering a parallel heat transfer pathway from the base of the droplet to the substrate surface [Fig. 5(b)], given by

$$\Delta T_{P2} = T_{b1} - T_s = \frac{q}{\pi R^2 k_{HC}\sin^2\theta}\left[\frac{k_P\varphi}{\delta_{HC}k_P + hk_{HC}} + \frac{k_w(1-\varphi)}{\delta_{HC}k_w + hk_{HC}}\right]^{-1}. \quad (8)$$

If the droplet morphology is S, the conduction temperature drop given by Eq. (8) becomes the S pillar temperature drop (including the coating temperature drop) where k_w = 0 W/mK. This signifies that there is no liquid bridge available for heat flow, leaving only the pillar structure.

By combining all of the temperature drops and determining the individual droplet heat transfer rate, q, gives

$$q = \frac{\pi R^2\left(\Delta T - \frac{2T_{sat}\sigma}{Rh_{fg}\rho_w}\right)}{\frac{1}{2h_i(1-\cos\theta)} + \frac{R\theta}{4k_w\sin\theta} + \frac{1}{k_{HC}\sin^2\theta}\left[\frac{k_P\varphi}{\delta_{HC}k_P+hk_{HC}} + \frac{k_w(1-\varphi)}{\delta_{HC}k_w+hk_{HC}}\right]^{-1}}, \quad (9)$$

The first, second and third terms in the denominator represent the liquid-vapor interface (R_i), droplet conduction (R_d), and pillar-coating-gap (P-C-G) thermal resistances (R_p, R_{hc}, R_g) respectively. The heat transfer rate can also be related to the droplet growth rate dR/dt using the relation $q = \dot{m}h_{fg}$,

$$q = \rho_w h_{fg}\frac{dV}{dt} = \frac{\pi}{3}\rho_w h_{fg}\frac{d}{dt}\{(1-\cos\theta)^2(2+\cos\theta)R^3\}. \quad (10)$$

EXPERIMENTAL AND MODELING RESULTS

During early stages of growth ($\langle R\rangle$ < 6 μm), the conduction resistance (R_d) is negligible compared to the other thermal resistances. Therefore, for the PW droplet, the pillar structure (R_p + R_{hc}) and liquid bridge (R_g + R_{hc}) resistances are dominant. However, in the S droplet, only the resistance associated with the pillar structure (R_p + R_{hc}) exists, which results in a higher total thermal resistance and 6× lower initial growth rate. Note that the P-C-G thermal resistance is not the only reason for the growth behavior difference between the two droplet morphologies, the higher initial contact angle of S morphology contributes to its slower growth rate due to lower droplet basal contact area.

As both droplet morphologies reach a critical radius, $R_{cd} \approx 6$ μm, the conduction resistance (R_d) dominates and limits the growth rate in both cases [18]. A theoretical estimate of R_{cd} was obtained by balancing the conduction resistance through the droplet, $R_d = R\theta/(4\pi R^2 k_w \sin\theta)$, with the interfacial, $R_i = 1/[2\pi R^2 h_i(1-\cos\theta)]$ and P-C-G, $R_{P-C-G} \sim k_P\varphi/[k_{HC}\pi R^2\sin^2\theta\,(\delta_{HC}k_P + hk_{HC})]$ thermal resistances. The interfacial and conduction resistances become equivalent at $R_{cd} = 4k_w\sin\theta\,(R_i + R_{P-C-G})/\theta \approx 6$ μm, which is in good agreement with our experiments. Figures 6(a) and (b) show the results from the model (red lines) and are in excellent agreement with the experiments.

Copyright © 2012 by ASME

Downloaded From: https://proceedings.asmedigitalcollection.asme.org on 01/09/2019 Terms of Use: http://www.asme.org/about-asme/terms-of-use

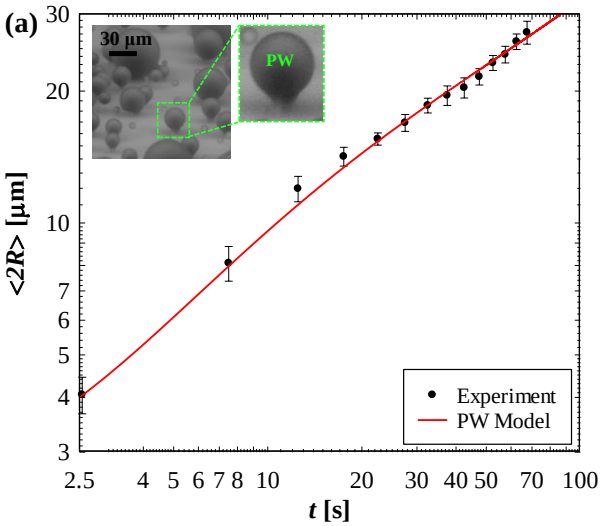

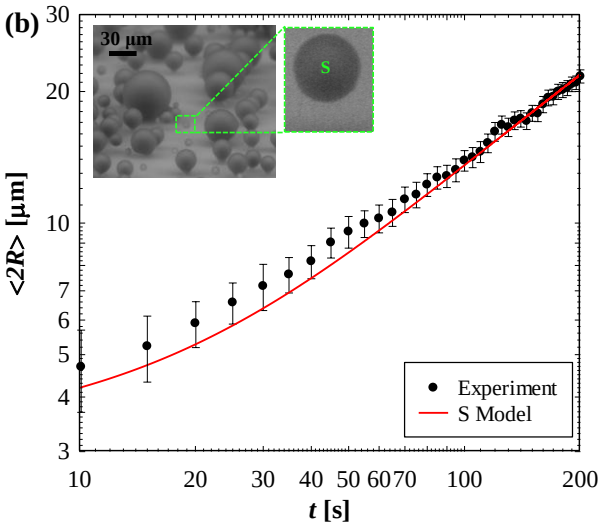

Fig. 6. *Time evolution of average droplet diameter (⟨2R⟩) for (a) the PW droplet. At early stages (⟨2R⟩ < 12 µm), the rapid droplet growth is due to good thermal contact between the droplet base and the substrate surface (T_s). Inset: (Top Left) ESEM example image of a PW droplet. (b) The S droplet. The S droplet has a slower growth rate than the PW droplet due to poor thermal contact between the base and substrate. At later stages (⟨2R⟩ ≥ 12 µm), the S and PW growth rates converge due to conduction thermal resistance (R_d) that dominates between the droplet interface and base. Experimental data (black circles) were obtained from ESEM video (P = 1200 ± 12 Pa, T_s = 282 ± 1.5 K). Inset: (Top Left) ESEM example image of a S droplet.*

HEAT TRANSFER ANALYSIS

Rapid droplet growth rates prior to droplet coalescence and removal are desired to enhance condensation heat transfer [1]. Therefore, PW droplet morphologies are desired. To estimate the heat transfer enhancement of the PW compared to the S droplets, the droplet heat transfer was obtained for each mode by integrating Eq. (10) from nucleation ($R = R^* \approx 0$) to coalescence ($R = l_c/2$.), and dividing by the time to reach coalescence (τ). A comparison of the heat transfers $\overline{q_{PW}}$ and $\overline{q_S}$ for the PW and S individual droplets, is given by

$$\frac{\overline{q_{PW}}}{\overline{q_S}} = \frac{\frac{Q_{PW}}{\tau_{PW}}}{\frac{Q_S}{\tau_S}}, \tag{11}$$

$$\frac{\overline{q_{PW}}}{\overline{q_S}} \cong \frac{(1-\cos\theta_{PW})^2(2+\cos\theta_{PW})\tau_S}{(1-\cos\theta_S)^2(2+\cos\theta_S)\tau_{PW}}, \tag{12}$$

where θ_{PW} and θ_S are the PW and S contact angles at coalescence, respectively, l_c is the coalescence length or coalescing droplet diameter, and τ_{pw} and τ_s are the PW and S droplet coalescence times (times at which coalescence occurs) corresponding to a coalescence length of l_c, respectively.

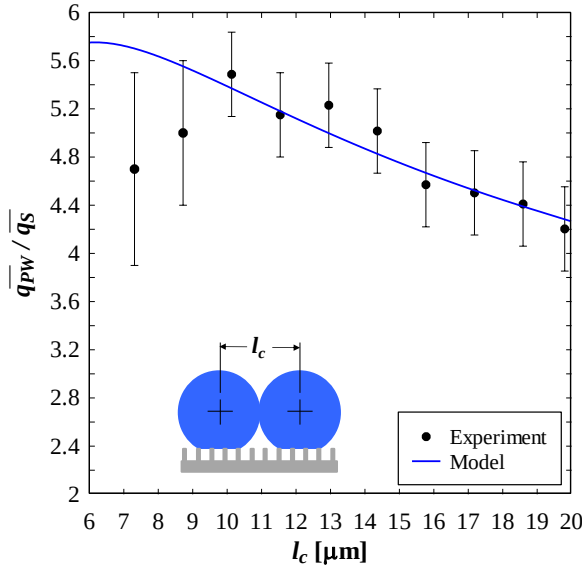

Fig. 7. *Heat transfer ratio of PW to S droplet versus coalescence length (l_c). The PW droplet is more than 4 times as effective as the S droplet at removing heat during the dropwise condensation process due to better thermal contact between the droplet base and substrate. The large contact angle of both droplet modes results in small pinning forces on the droplet contact line, resulting in spontaneous droplet removal at an average coalescence length of 10 ± 2 µm. Inset: Coalescence length definition schematic.*

It is important to note, the heat transfer ratio is valid for the two droplet morphologies (PW and S), not for two different surfaces. Fig. 7 shows the results from the experiments and the model, which demonstrate a 4-6× increase in heat transfer during dropwise condensation of PW droplets compared to S droplets. The heat transfer enhancement diminishes at larger coalescence lengths due to increasing droplet conduction thermal resistance for both PW and S droplets, resulting in identical growth rates.

Copyright © 2012 by ASME

Downloaded From: https://proceedings.asmedigitalcollection.asme.org on 01/09/2019 Terms of Use: http://www.asme.org/about-asme/terms-of-use

FLAT SURFACE COMPARISON

Flat Surface Growth Experiments

To obtain an estimate of heat transfer performance enhancement due to nanostructuring, additional growth studies were performed on a flat surface. The flat surface sample consisted of a silicon substrate, functionalized by chemical vapour deposition (CVD) of (tridecafluoro-1,1,2,2-tetrahydrooctyl)-1-trichlorosilane. Droplet growth on the flat surface was characterized using identical condensation conditions as the nanostructured surface. Fig. 8 shows individual droplet growth of the three distinct droplet morphologies, PW, S, and flat (F). Droplets on the flat sample nucleate randomly on the surface and grow with an approximately constant contact angle of $\theta_F = 120°$, which is in good agreement with the advancing contact angle θ_a = 119.2° ± 1.3° measured using the micro-goniometer.

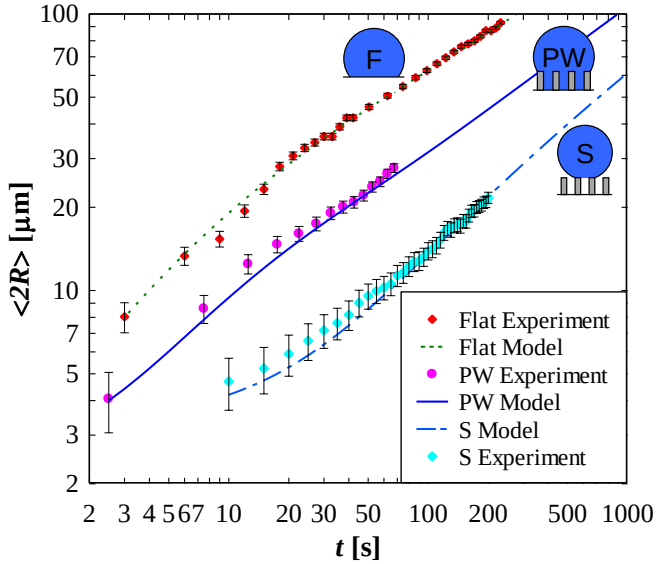

Fig. 8. *Time evolution of average droplet diameter (⟨2R⟩) for the PW, S and flat droplet morphologies. At later stages (⟨2R⟩ ≥ 12 μm), the droplet growth rates converge due to dominating conduction thermal resistance (R_d) between the droplet interface and base.*

The growth rate of F droplets is higher than that of PW or S morphologies due to the lower contact angle. Additionally, the P-C-G thermal resistance is not present on the flat surface, further enhancing growth. However, the higher growth leads to higher droplet pinning and larger droplet removal sizes. The average coalescence length of F droplets is found to be l_c = 30 ± 2 μm [Fig 9].

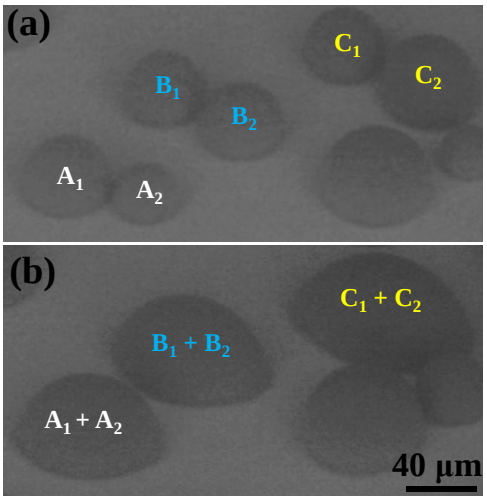

Fig. 9. *Droplet coalescence on the flat surface for 3 separate droplet pairs (a) immediately before and (b) immediately after coalescence. The average coalescence diameter for F droplets is l_c = 30 ± 2 μm.*

Heat Flux Model

To provide a direct comparison of heat transfer performance between the flat and nanostructured surface morphologies, we integrated the thermal resistance model with droplet size distribution theory. For small droplets, the size distribution *n(R)* is determined as [17, 23]

$$n(R) = \frac{1}{3\pi R^2 \hat{R}}\left(\frac{R_e}{\hat{R}}\right)^{-\frac{2}{3}} \frac{R(R-R^*)}{R-R^*} \frac{A_2 R + A_3}{A_2 R_e + A_3} \exp(B_1 + B_2), \quad (13)$$

where

$$B_1 = \frac{A_2}{\tau A_1}\left[\frac{{R_e}^2 - R^2}{2} + R^*(R_e - R) - {R^*}^2 \ln\left(\frac{R-R^*}{R_e-R^*}\right)\right], \quad (14)$$

$$B_2 = \frac{A_2}{\tau A_1}\left[R_e - R - R^* \ln\left(\frac{R-R^*}{R_e-R^*}\right)\right], \quad (15)$$

$$\tau = \frac{3{R_e}^2(A_2 R_e + A_3)^2}{A_1\left(11A_2{R_e}^2 - 14A_2 R_e R^* + 8A_3 R_e - 11A_3 R^*\right)}, \quad (16)$$

$$A_1 = \frac{\Delta T}{h_{fg}\rho_w(1-\cos\theta)^2(2+\cos\theta)}, \quad (17)$$

$$A_2 = \frac{\theta}{4k_w \sin\theta}, \quad (18)$$

$$A_3 = \frac{1}{2h_i(1-\cos(\theta))} + \frac{1}{k_{HC}\sin^2\theta}\left[\frac{k_P \varphi}{\delta_{HC}k_P + hk_{HC}} + \frac{k_w(1-\varphi)}{\delta_{HC}k_w + hk_{HC}}\right]^{-1}. \quad (19)$$

For large droplets which grow mainly due to coalescence, the droplet distribution *N(R)* is governed by [24]

$$N(R) = \frac{1}{3\pi R^2 \hat{R}}\left(\frac{R_e}{\hat{R}}\right)^{-\frac{2}{3}}. \quad (20)$$

Copyright © 2012 by ASME

Downloaded From: https://proceedings.asmedigitalcollection.asme.org on 01/09/2019 Terms of Use: http://www.asme.org/about-asme/terms-of-use

The effective maximum droplet radius, $\hat{R}$, is assumed to be 2 mm [17]. The effective radius R_e is defined as the radius when droplets growing by direct vapor addition begin to merge and grow by droplet coalescence. Assuming nucleation sites form a square array, the effective radius is

$$R_e = \frac{1}{\sqrt{4N_s}}\ , \qquad (21)$$

where N_s is the number of nucleation sites per unit area of condensing surface. The drop size distribution obtained from Eqns. (13) and (20) is shown in Fig. 10 for four different nucleation densities. Higher nucleation densities result in lower effective radii, and higher distributions of small droplets on the surface.

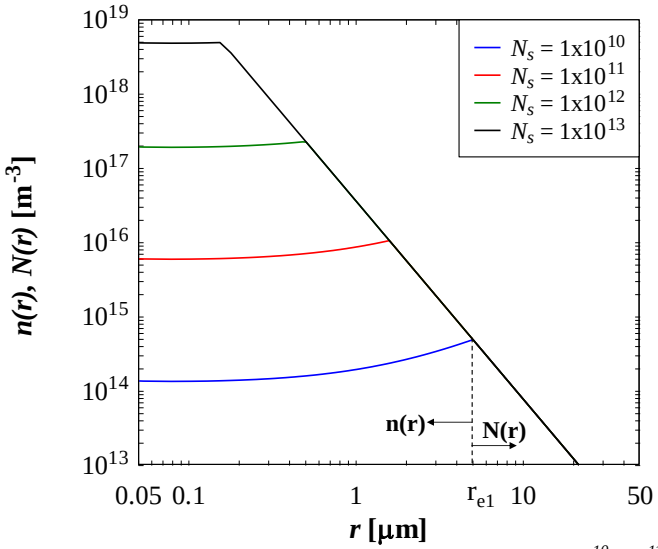

Fig. 10. *Drop size distribution for nucleation densities of 10^{10}, 10^{11}, 10^{12}, and 10^{13} m^{-2}.*

The steady state condensation heat flux is obtained by multiplying the individual heat transfer rate through a single droplet (Eq. (9)) with the droplet size distribution (Eqns. (13) and (20)) and integrating the result over all radii given by

$$q'' = \int_{R^*}^{R_e} q(R)n(R)dR + \int_{R_e}^{R_{max}} q(R)N(R)dr\ . \qquad (22)$$

Comparison Results

Equation (22) is used to determine the heat flux performance for surfaces having each droplet morphology (PW, S and F) individually. In order to compare the effects of nanostructuring, the droplet coalescence length, l_c, which is equivalent to the effective radius, R_e, is changed by varying the nucleation density. Each calculated heat flux is compared to the baseline flat surface performance, which assumes a constant l_c = 30 μm, and departure radius of $\hat{R}$ = 2 mm. For the nanostructured surface, growth beyond the coalescence length is assumed to be non-existent due to droplet coalescence induced removal from the surface. The sweeping time τ is assumed to be infinite, and $l_c = \hat{R} = R_e$ = 10 μm. Figure 11 shows the heat transfer ratio of each surface as a function of coalescence length. As l_c decreases, heat transfer performance increases markedly due to a smaller departure size, and larger droplet density of smaller 'active' droplets. As expected, the PW morphology shows an enhancement in heat transfer when compared to the S morphology for all l_c due to faster growth with identical droplet distributions. However, the PW enhancement over the flat surface is only valid for l_c < 19 μm. Beyond this departure size, the flat surface has a higher heat flux, indicating a limit to coalescence induced droplet removal heat transfer enhancement for this particular surface. Additionally, the S morphology surface always shows degradation when compared to the flat surface, *i.e.*, the addition of the P-C-G resistance hinders growth and dominates over the heat transfer enhancement gained from coalescence induced droplet removal. For this particular surface, l_c = 10 μm, indicating a 56% heat transfer enhancement for the PW wetting morphology, and 71% degradation in performance for the S morphology when compared to the flat surface.

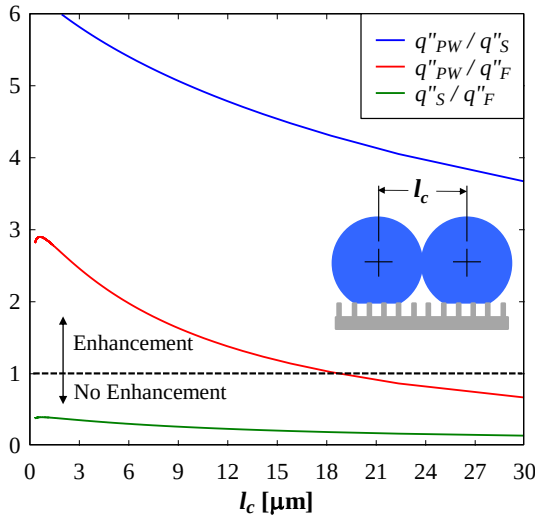

Fig. 11. *Heat flux ratio as a function of droplet coalescence length for surfaces with PW, S and F droplet morphologies. S morphology surface shows no enhancement when compared to the F surface for all coalescence lengths. The PW morphology surface shows increased enhancement as l_c decreases below 19 μm.*

To gain an understanding of the effect of droplet morphology on total surface heat flux, the pillar height h in the resistance model was varied, for a constant solid fraction φ = 0.0177 [Fig. 12]. The heat transfer ratio diminishes for decreasing h due to the vanishing discrepancy in the P-C-G thermal resistance between the two morphologies. As h approaches zero, the ratio does not approach 1 due to the initial contact angle difference between the two morphologies. For larger l_c, the ratio decreases due to conduction resistance (R_c) limited droplet growth, eliminating any initial enhancement obtained by having early departure of droplets.

Copyright © 2012 by ASME

Downloaded From: https://proceedings.asmedigitalcollection.asme.org on 01/09/2019 Terms of Use: http://www.asme.org/about-asme/terms-of-use

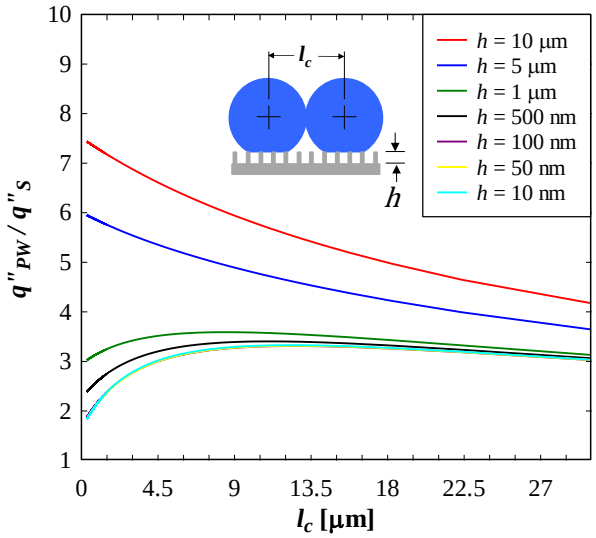

Fig. 12. *Heat flux ratio of the PW surface to the S surface as a function of droplet coalescence length, l_c. For the nanostructured surface the coalescence length is the departure length, R_e.*

A similar comparison is done between the PW and F surface for decreasing values of h [Fig 13]. As expected, the heat flux ratio increases as h decreases due to the diminishing P-C-G thermal resistance. It is important to note, as the coalescence length scale approaches ~100 nm, the heat flux ratio decreases sharply. This result is due to the droplet curvature resistance (R_c) which becomes dominant at small length scales.

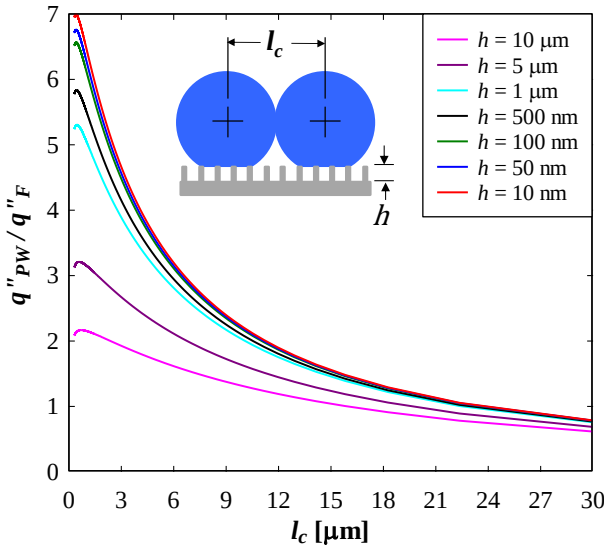

Fig. 13. *Heat flux ratio of the PW surface to the F surface as a function of droplet coalescence length, l_c. For the PW surface, the coalescence length is the departure length, R_e.*

Figure 14 shows the heat flux (q'') as a function of ΔT between the saturated vapor and substrate surface. For the experimental conditions in this study (l_c = 10 ± 2 μm), the results clearly show the performance enhancement created by surface nanostructuring which results in droplets forming in the PW morphology. However, depending on the morphology, nanostructuring can deteriorate the surface heat flux when compared to a flat silanated surface if the nucleated droplets maintain the S morphology.

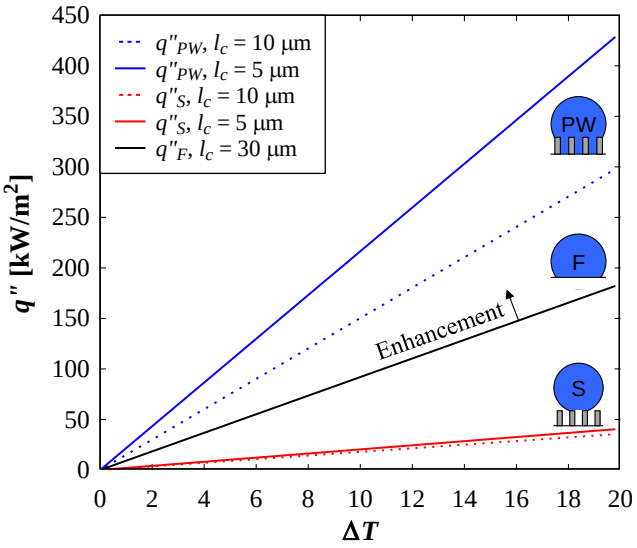

Fig. 14. *Heat flux (q'') versus temperature difference (ΔT) for surfaces having distinct PW, S and F droplet morphologies (h = 6.1 μm, l = 2 μm, d = 300 nm, φ = 0.0177, P = 4000 Pa). Heat flux enhancement occurs for PW morphologies, while degradation occurs for S morphologies.*

CONCLUSIONS

In summary, we show the importance of droplet wetting morphology on condensing growth rate on Cassie stable surfaces *via* an *in situ* ESEM study of a coexisting of S and PW morphologies on a superhydrophobic structured surface. The PW wetting mode was shown to have a 6× higher initial growth rate than the S mode due to the increased contact with the substrate. Experiments were validated using an analytical heat transfer model, and are in good agreement. Calculation of the heat transfer ratio of PW to S wetting morphologies for varying droplet coalescence lengths shows the heat transfer of the PW droplets to be 4-6× more effective. To compare the heat transfer enhancement, PW and S droplet heat flux is compared to that of a flat superhydrophobic silane coated surface, showing a 56% enhancement for the PW morphology, and 71% degradation for the S morphology. This study provides insight into the hereto unidentified importance of local wetting morphology on droplet growth rate during superhydrophobic condensation, as well as the importance of designing CB stable surfaces with PW droplet morphologies to achieve enhanced heat during dropwise condensation.

Copyright © 2012 by ASME

Downloaded From: https://proceedings.asmedigitalcollection.asme.org on 01/09/2019 Terms of Use: http://www.asme.org/about-asme/terms-of-use

NOMENCLATURE

d	Pillar diameter [m]
E^*	Wetting-state energy ratio [-]
h	Pillar height [m]
h_{fg}	Latent heat of vaporization [J/kg]
h_i	Liquid-vapor interface heat transfer coeff. [W/m·K]
k_{HC}	Hydrophobic coating thermal conductivity [W/m·K]
k_P	Pillar/substrate thermal conductivity [W/m·K]
k_w	Water thermal conductivity [W/m·K]
l	Pillar center-to-center spacing [m]
l_c	Coalescence length [m]
$\dot{m}$	Mass rate of condensate formation [kg/s]
N	Large droplet population density [m^{-3}]
n	Small droplet population density [m^{-3}]
N_s	Number of nucleation sites per unit area [m^{-2}]
P	Vapor saturation pressure [Pa]
q	Individual droplet heat transfer [W]
$\overline{q_{PW}}$	Partially wetting morphology drop heat transfer [W]
$\overline{q_S}$	Suspended morphology drop heat transfer [W]
q''	Heat flux [W/m^2]
r	Surface roughness [-]
R	Droplet radius [m]
R^*	Minimum droplet nucleation radius [m]
$\hat{R}$	Effective maximum droplet radius [m]
$\langle R \rangle$	Average experimental droplet radius [m]
R_e	Droplet interaction radius [m]
R_c	Droplet curvature thermal resistance [K/W]
R_{cd}	Critical radius when $R_c = R_i$ [m]
R_i	Liquid-vapor interfacial thermal resistance [K/W]
R_d	Droplet conduction thermal resistance [K/W]
R_{hc}	Hydrophobic coating thermal resistance [K/W]
R_p	Pillar structure thermal resistance [K/W]
R_g	Pinned liquid region thermal resistance [K/W]
$\bar{R}$	Gas constant [J/mol·K]
S	Suspended [-]
t	Time [s]
ΔT	Surface subcooling temperature [K]
ΔT_c	Droplet curvature temperature drop [K]
ΔT_{HC}	Coating layer conduction temperature drop [K]
ΔT_i	Liquid-vapor interfacial temperature drop [K]
ΔT_d	Droplet body conduction temperature drop [K]
$\Delta T_{P,S}$	Suspended droplet pillar temperature drop [K]
ΔT_{P2}	Pillar, coating and gap temperature drop [K]
T_{b1}	Liquid temperature at the droplet base [K]
T_{b2}	Temperature of pillar tops beneath coating [K]
T_i	Liquid-vapor interfacial temperature [K]
T_{sat}	Vapor saturation temperature [K]
T_s	Substrate/wall temperature [K]
T_s'	Substrate subcooled region temperature [K]
V	Volume [m^3]
W	Wenzel [-]

Greek Symbols

α	Condensation coefficient [-]
θ	Contact angle [°]
φ	Solid fraction [-]
σ	Surface tension [N/m]
ρ_w	Water density [kg/m^3]
v_g	Water vapor specific volume [m^3/kg]
δ	Thickness [m]
τ	Sweeping period, [s]
τ_{PW}	Partially wetting droplet coalescence time [s]
τ_S	Suspended droplet coalescence time [s]

Superscript

CB	Cassie-Baxter
PW	Partially wetting

Subscripts

a	Advancing
c	Curvature, critical, coalescence
CB	Cassie Baxter
d	Droplet
e	Equilibrium, effective
F	Flat
g	Pinned liquid region under droplet
HC	Hydrophobic coating
i	Liquid-vapor interface
p	Pillar
PW	Partially wetting
P-C-G	Pillar, coating, pinned liquid region
r	Receding
S	Suspended
w	Water

ACKNOWLEDGMENTS

N. M. and E. N. W. acknowledge supported from the MIT S3TEC Center, and Energy Frontier Research Center funded by the Department of Energy, Office of Science, Office of Basic Energy Sciences. N. M. would also like to acknowledge funding support from the Natural Sciences and Engineering Research Council of Canada. R.E. acknowledges support from the Irish Research Council for Science, Engineering, and Technology, cofunded by Marie Curie Actions under FP7. This work was performed in part at the Center for Nanoscale Systems (CNS), a member of the National Nanotechnology Infrastructure Network (NNIN), which is supported by the National Science Foundation under NSF award no. ECS-0335765. CNS is part of Harvard University.

REFERENCES

[1] J. B. Boreyko and C. H. Chen, "Self-Propelled Dropwise Condensate on Superhydrophobic Surfaces," *Physical Review Letters*, vol. 103, pp. -, Oct 30 2009.

[2] C. H. Chen, *et al.*, "Dropwise condensation on superhydrophobic surfaces with two-tier roughness," *Applied Physics Letters*, vol. 90, pp. -, Apr 23 2007.

[3] C. Dietz, *et al.*, "ESEM Imaging of Condensation on a Nanostructured Superhydrophobic Surface," *Journal of Heat Transfer-Transactions of the Asme*, vol. 132, pp. -, Aug 2010.

Copyright © 2012 by ASME

Downloaded From: https://proceedings.asmedigitalcollection.asme.org on 01/09/2019 Terms of Use: http://www.asme.org/about-asme/terms-of-use

[4] R. D. Narhe and D. A. Beysens, "Water condensation on a super-hydrophobic spike surface," *Europhysics Letters,* vol. 75, pp. 98-104, Jul 2006.
[5] K. K. Varanasi, *et al.*, "Spatial control in the heterogeneous nucleation of water," *Applied Physics Letters,* vol. 95, pp. -, Aug 31 2009.
[6] R. Enright, *et al.*, *Nature Materials,* 2011.
[7] N. Miljkovic, *et al.*, "Liquid Evaporation on Superhydrophobic and Superhydrophilic Nanostructured Surfaces," *Journal of Heat Transfer,* vol. 133, 2011.
[8] K. K. S. Lau, *et al.*, "Superhydrophobic carbon nanotube forests," *Nano Letters,* vol. 3, pp. 1701-1705, Dec 2003.
[9] B. Bhushan, *et al.*, "Nanostructures for superhydrophobicity and low adhesion," *Soft Matter,* vol. 4, pp. 1799-1804, 2008.
[10] R. N. Wenzel, "Resistance of Solid Surfaces to Wetting by Water," *ACS Industial & Engineering Chemistry,* vol. 29, pp. 988-994, 1936.
[11] K. Rykaczewski, *et al.*, "Electron beam heating effects during environmental scanning electron microscopy imaging of water condensation on superhydrophobic surfaces," *Applied Physics Letters,* vol. 98, pp. -, Feb 28 2011.
[12] K. Rykaczewski and J. H. J. Scott, *Acs Nano,* vol. 5, 2011.
[13] A. Lafuma and D. Quere, "Superhydrophobic states," *Nat Mater,* vol. 2, pp. 457-460, 2003.
[14] R. Xiao, *et al.*, "Prediction and Optimization of Liquid Propagation in Micropillar Arrays," *Langmuir,* vol. 26, pp. 15070-15075, 2010.
[15] S. Moulinet and D. Bartolo, "Life and death of a fakir droplet: Impalement transitions on superhydrophobic surfaces," *European Physical Journal E,* vol. 24, pp. 251-260, Nov 2007.
[16] C. Dietz, *et al.*, "Visualization of droplet departure on a superhydrophobic surface and implications to heat transfer enhancement during dropwise condensation," *Applied Physics Letters,* vol. 97, pp. -, Jul 19 2010.
[17] S. Kim and K. J. Kim, "Dropwise Condensation Modeling Suitable for Superhydrophobic Surfaces," *Journal of Heat Transfer,* vol. 133, 2011.
[18] H. Tanaka and T. Tsuruta, "A Microscopic Study of Dropwise Condensation," *International Journal of Heat and Mass Transfer,* vol. 27, pp. 327-335, 1984.
[19] D. Tam, *et al.*, "Marangoni convection in droplets on superhydrophobic surfaces," *Journal of Fluid Mechanics,* vol. 624, pp. 101-123, Apr 10 2009.
[20] V. P. Carey, *Liquid-vapor phase-change phenomena : an introduction to the thermophysics of vaporization and condensation processes in heat transfer equipment*, 2nd ed. New York: Taylor and Francis, 2008.
[21] R. W. Schrage, "A theoretical study of interphase mass transfer," Thesis, Columbia University., New York,, 1953.
[22] A. Umur and P. Griffith, "Mechanism of Dropwise Condensation," *Journal of Heat Transfer,* vol. 87, pp. 275-&, 1965.
[23] M. AbuOrabi, "Modeling of heat transfer in dropwise condensation," *International Journal of Heat and Mass Transfer,* vol. 41, pp. 81-87, Jan 1998.
[24] J. W. Rose, *International Journal of Heat and Mass Transfer,* vol. 10, 1967.

Copyright © 2012 by ASME

Downloaded From: https://proceedings.asmedigitalcollection.asme.org on 01/09/2019 Terms of Use: http://www.asme.org/about-asme/terms-of-use